CHAPTER SEVEN

Electrical and superconducting transport in topological insulator nanoribbons

Morteza Kayyalha[1], Leonid P. Rokhinson[2,3,*] and Yong P. Chen[2,3]
[1]Department of Electrical Engineering, Pennsylvania State University, University Park, PA, United States
[2]Department of Physics and Astronomy, Purdue University, West Lafayette, IN, United States
[3]Department of Electrical and Computer Engineering, Purdue University, West Lafayette, IN, United States
*Corresponding author: leonid@purdue.edu

1. Introduction

In solid state physics, materials are divided into two distinct categories: metals, such as gold, and insulators, such as SiO_2. This distinction is based on whether the Fermi energy resides inside the conduction/valence bands (metals) or inside the bandgap (insulators). However, discovery of the integer quantum Hall (QH) effect, which is insulating in bulk whilst conducting along the edges, rattled this distinction. The study of the QH effect has led to a new classification of materials: topological materials [1,2]. In the QH insulator, an external magnetic field breaks the time reversal symmetry and creates Landau levels. The QH states belong to different topological classes compared to the trivial insulators. When insulators from two different topological classes are placed next to each other, the insulating gap must close at their boundary giving rise to edge modes (in two dimensions) and surface states (in three dimensions). In a sense, comparing the topology of a nontrivial band structure and a trivial one is analogous to comparing a rubber band and a Möbius strip; one cannot be smoothly deformed into the other without breaking [2]. The closing of the bandgap at the boundary of topological and trivial insulators is hence analogous to the 'breaking' of the rubber band and converting it into the Möbius strip. This 'topological transition' makes the edge/surface states independent of the material details and insensitive to any smooth deformation of the system. Over the past few years, several topological states of matter, including two-dimensional (2D) [3] and three-dimensional (3D) topological insulators (TIs) [1,2], topological crystalline insulators [4], topological Dirac semimetals and Weyl semimetals [5,6], have been theoretically predicted and experimentally

Semiconductor Nanodevices
ISBN: 978-0-12-822083-2
https://doi.org/10.1016/B978-0-12-822083-2.00004-6

verified. In this chapter, we focus on 3D TIs, including TI nanoribbons (TINRs), and discuss their electrical and superconducting transport properties.

TIs belong to a class of topological materials where time reversal symmetry is preserved. A strong spin–orbit coupling (SOC) and band inversion in the TI results in the appearance of a nontrivial insulating bulk bandgap and topologically protected surface states. The topological protection refers to the immunity of surface states against backscattering by nonmagnetic impurities such as crystalline defects, and surface roughness [1,2,7]. These topological surface states (TSSs) are spin-helical states with linear Dirac fermion-like energy–momentum dispersion. Early examples of 3D TIs are Bi_2Se_3, Bi_2Te_3, Sb_2Te_3 and their compounds [1,2]. These materials are amongst the most commonly used thermoelectric materials and have been studied extensively over the years [8]. However, only recently, topological origin of thermoelectric and electronic properties became understood. Other examples of 3D TIs include strained HgTe [9] and SmB_6 [10].

Fig. 7.1a and b depict schematics of the surface band dispersion in momentum space and spin texture of the TSS in a real space, respectively. Due to the strong SOC, spin of charge carriers in the TSS is locked perpendicular to the momentum and tangential to the surface. Therefore, the spin-helical TSS may give rise to the current/momentum-induced spin polarisation and, hence, have many potential applications in spintronics [11,12]. Moreover, ferromagnetic doping of the TIs can open an exchange gap in TSS, leading to the quantum anomalous Hall effect [13,14] or topological magnetoelectric effect [15]. The TSS coupled to a conventional superconductor may give rise to the topological superconductivity and Majorana modes [1,16], top candidates to create a fault-tolerant qubit.

This chapter is organised as follows: we will first overview some of the electrical transport signatures of TSS in 3D TIs. We will then introduce

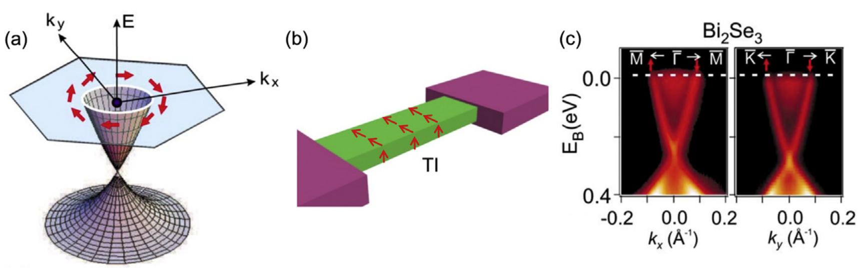

Figure 7.1 (a) Schematic of spin-helical surface energy dispersion of a typical 3D TI. (b) Schematic of the spin texture in a 3D TI surface state. Spin is always tangential to the surface and perpendicular to the momentum. (c) Band structure of Bi_2Se_3 measured by ARPES. *Credit: Adapted from Refs. [1,17,42].*

the TINR as an interesting candidate for the observation of topological transport. Finally, we will present recent progress in combining 3D TINR and superconductors in pursuit of topological superconductivity and Majorana modes.

2. Overview of electrical transport in TI

The band dispersion of a 3D TI has been measured by an angle resolved photoemission spectroscopy (ARPES) on Bi_2Se_3 samples [1,17]. Fig. 7.1c shows the ARPES data, where linear spin-polarised Dirac dispersion of the TSS is demonstrated. In a perfect TI bulk is insulating and electrical current is carried by surface states. In reality, bulk carriers contribute to the conduction due to unintentional impurity doping and thermal excitations. There are several methods to separate the contributions of TSS and bulk carriers. Doping a conventional Bi_2Te_3, which is highly electron doped, with Sb shifts the chemical potential into the bandgap and compensates for the unintended doping. It was found that ternary and quaternary tetradymite TI materials, such as $(Bi,Sb)_2Te_3$ and $BiSbTeSe_2$, exhibit a very low bulk contribution [18–21]. For instance, the sheet resistance R_{sh} in $BiSbTeSe_2$ does not change with the thickness (see Fig. 7.2a) [22], suggesting that R_{sh} is completely dominated by the TSS contribution at $T = 2$ K and the bulk is insulating. We note that in conventional metals sheet resistance is inversely proportional to the thickness.

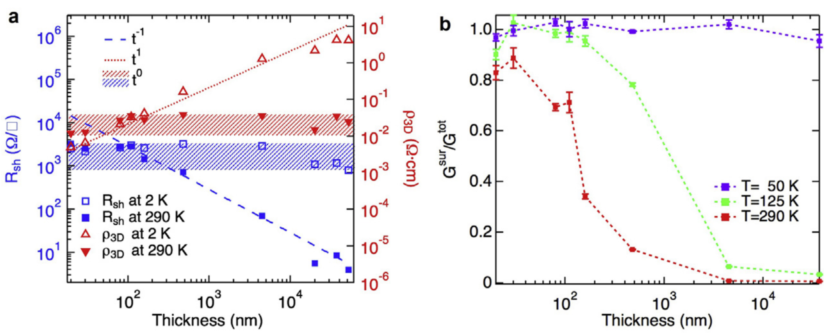

Figure 7.2 (a) Sheet resistance R_{sh} and 3D resistivity ρ_{3D} in $BiSbTeSe_2$ versus thickness at $T = 2$ K and $T = 295$ K. At $T = 2$ K, R_{sh} exhibits a 2D behaviour and does not change with the thickness. The dashed blue (dark grey in print version) line and the horizontal red (grey in print version) band represent the expected behaviours for R_{sh} and ρ_{3D} of a 3D bulk conductor, respectively. (b) TSS contribution to the total conductance (G^{sur}/G^{tot}) versus thickness at three temperatures. *Credit: Ref. [22].*

2.1 Temperature dependence of the electrical conductivity

For TIs with the Fermi energy residing within the gap, we expect that contribution of bulk conduction will be suppressed at low temperatures. Therefore, the temperature dependence of the electrical conductivity can provide insight into the nature of electrical transport and, consequently, reveal the contribution of the TSS. The surface contribution to the total conductance can be extracted from the temperature-dependent electrical conductivity using a simple model developed in Ref. [23]. In this model, the total sheet conductance is a sum of a thermally activated bulk conductance and a metallic surface conductance $G^{tot}(T) = G^{bulk}(T) + G^{sur}$, where $G^{bulk} = t\sigma_{0b}\exp\left(-\frac{E_g}{k_BT}\right)$, t is the thickness of the TI, σ_{0b} is the high temperature conductivity of the bulk, E_g is the bulk gap, k_B is the Boltzmann constant and T is the temperature. The metallic surface contribution can be modelled as $G^{sur} = 1/(R_{s0} + AT)$, where R_{s0} accounts for the residual resistance at $T = 0$ K and A introduces electron–phonon coupling [23]. The model predicts that for temperatures $k_BT < E_g$, G^{tot} is dominated by G^{sur} and increases with decreasing temperature. This model was employed by Y. Xu et al. [22] to estimate the surface to bulk contribution in $BiSbTeSe_2$ films. Fig. 7.2b plots the extracted surface contribution to the total conductance versus thickness. The authors observed that at low temperatures or in thin flakes conductance is mostly dominated by the surface contribution.

2.2 3D TI in a perpendicular magnetic field

2.2.1 *Low magnetic field range: weak anti-localisation*

In a strong spin orbit-coupled system, such as a TI, magnetoconductance is expected to exhibit weak anti-localisation (WAL). WAL originates from destructive quantum interference of self-intersecting scattering paths due to spin–momentum coupling. When a small magnetic field is applied, time reversal symmetry is broken and WAL is suppressed. Therefore, at low magnetic fields (B) conductance decreases with an increase of magnetic field, and negative magnetoconductance $\Delta\sigma(B) = \sigma(B) - \sigma(0)$ with a characteristic cusp at $B = 0$ T is observed. The WAL can be modelled using the Hikami–Larkin–Nagaoka formula [24]:

$$\Delta\sigma(B) = -\alpha\frac{e^2}{2\pi^2\hbar}\left[\ln\left(\frac{\hbar}{4el_\varphi^2B}\right) - \Psi\left(\frac{\hbar}{4el_\varphi^2B} + \frac{1}{2}\right)\right], \tag{7.1}$$

where Ψ is the digamma function, l_φ is the phase coherence length and α is a numeric prefactor. For a linear Dirac dispersion of the TSS, which has a Berry phase of π, $\alpha = -0.5$. In a TI film, however, there are two parallel surfaces (top and bottom), each contributing -0.5 to α. Therefore, for transport which involves both TSS $\alpha = -1$. The value of α was recently extracted from magnetoconductance measurements in gate-tunable $BiSbTeSe_2$ flakes by Y. Xu et al. [22,25]. Fig. 7.3 depicts the gate dependence of the longitudinal resistance R_{xx} in $BiSbTeSe_2$ flakes at zero magnetic field, where a peak in the resistance is observed close to the back-gate voltage $V_{bg} = -60$ V. This gate voltage highlights the position of the chemical potential where the total charge in the system is neutral and, hence, is called a charge neutrality point (CNP). Fig. 7.3b and c depict magnetoconductance and the extracted α and l_φ in the TI flakes. When both the top and the bottom surfaces are electron doped, which is the case for $V_{bg} > -30$ V, $\alpha \approx -1.2$. Near the charge CNP or for the case when the top surface is electron doped and the bottom surface is hole doped ($V_{bg} < -30$ V), α is further reduced. The reason behind this deviation is not clear to us.

2.2.2 High magnetic field range: half-integer QH effect

When a TI is exposed to a strong perpendicular magnetic field, Landau levels are formed. In conventional semiconductors, because of the parabolic nature of the band dispersion, the Landau quantisation produces equidistant energy levels and gives rise to the integer QH effect, manifested by quantised Hall conductivity and zero longitudinal conductivity [26–30]. For relativistic carriers with linear Dirac dispersion, Landau levels are not equidistant and, more importantly, the Hall conductivity is quantised at half integers

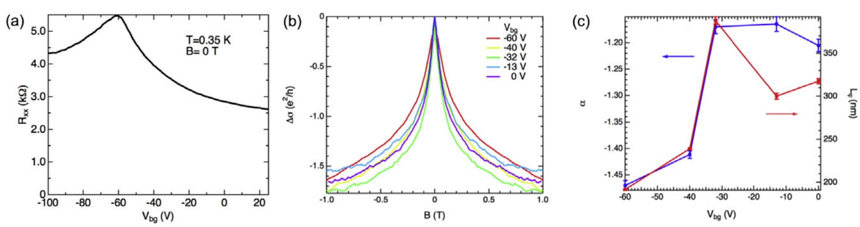

Figure 7.3 Longitudinal resistance R_{xx} as a function of the back-gate voltage V_{bg} at $T = 0.35$ K and $B = 0$ T. (b) Magnetoconductance $\Delta\sigma$ versus magnetic field for various back-gate voltages, marking the weak anti-localisation effect. (c) α and l_φ versus V_{bg}. All measurements are done in $BiSbTeSe_2$ flakes obtained by the scotch tape exfoliation from a bulk crystal. *Credit: Refs. [22,25].*

[15,22,31]. A half-integer QH effect was first observed in gate-tunable $BiSbTeSe_2$ flakes by Y. Xu et al. [22] and was later reproduced by others [32,33]. Fig. 7.4a presents a longitudinal resistance $R_{xx} = V_{2,3}/I_{1,4}$, where subscripts correspond to different terminals as shown in the inset, and a Hall resistance $R_{xy} = V_{5,3}/I_{1,4}$ as functions of the back-gate voltage V_{bg} at $T = 0.35$ K in the same $BiSbTeSe_2$ flake as the one shown in Fig. 7.3. Fig. 7.4b depicts the calculated longitudinal (σ_{xx}) and Hall conductivity (σ_{xy}) as functions of V_{bg}. At $V_{bg} = 0$ V, the sample is n-doped (both top and bottom surfaces) and due to the large thickness of the flake, the back-gate control over the top surface is negligible. Therefore, the top surface most likely remains n-doped throughout the V_{bg} range used in this study. When both the top and the bottom surfaces are electron doped ($V_{bg} > -60$ V), well-developed quantised plateaus in σ_{xy} accompanied by vanishing σ_{xx} are observed. The quantised values of σ_{xy} are integer values of e^2/h, where e is the electron charge and h is the Planck constant. This indicates that each surface of the TI flake contributes half-integer quantised conductance to the measured total conductivity. Moreover, the lack of gate control on the top surface ensures that the contribution from the top surface is always $\frac{1}{2}e^2/h$. The observed plateaus in this experiment can be understood as parallel contributions from the top surface ($\nu_t e^2/h$) and the bottom surface ($\nu_b e^2/h$). In other words, $\sigma_{xy}^{tot} = \sigma_{xy}^{top} + \sigma_{xy}^{bottom} = (\nu_t + \nu_b)e^2/h = (N_t + N_b + 1)e^2/h$, where $\nu_{t(b)} = N_{t(b)} + \frac{1}{2}$ is the Landau level filling factor and $N_{t(b)}$ is an integer number. In electron-doped bottom-gated TIs, ν_t is always ½

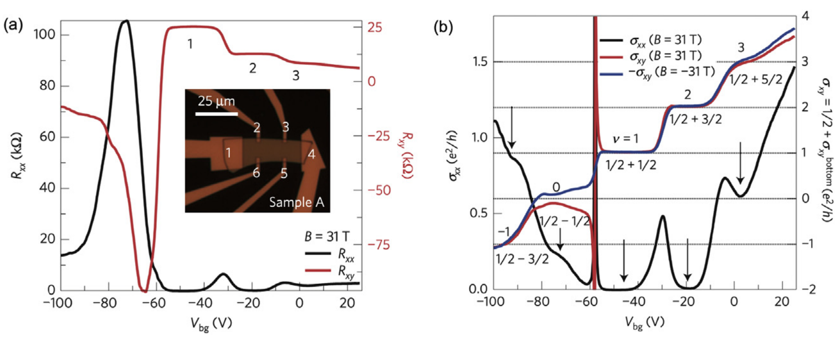

Figure 7.4 (a) Longitudinal (R_{xx}) and Hall (R_{xy}) resistance as functions of the back-gate voltage (V_{bg}) at $B = 31$ T and $T = 0.35$ K. Inset shows the optical image of the device where different electrodes are marked. (b) Calculated 2D longitudinal σ_{xx} and Hall σ_{xy} conductivities from (a). *Credit: Ref. [22].*

and, hence, $\sigma_{xy}^{tot} = (N_b + 1)e^2/h$ is always quantised. The top and bottom Landau level filling factors are marked for each plateau in Fig. 7.4b. In order to control ν_t, one needs to fabricate dual gated structures where both the top and bottom surfaces are controlled independently. This was accomplished by Yang Xu et al. in Ref. [34].

3. Electrical transport in TI nanoribbons

In this section, we introduce quantum interference effects in TSSs. Unlike bulk samples, in mesoscopic systems, e.g., TINR, the low temperature phase coherence length is comparable to the length scale of the sample and phase coherence transport can be observed. TINRs resemble a metallic hollow cylinder and electron trajectories can self-interfere when electrons move around the cross-sectional circumference. When a magnetic field along the length of a TINR is applied, quantum interference is affected by the magnetic flux [35]. As a result, the interference patterns will give rise to quantum oscillations of magnetoresistance as a function of the magnetic flux, with a characteristic period of the flux quantum, $\Phi_0 = h/e$ [36–39]. Such oscillations are known as Aharonov–Bohm (AB) effects and have been observed in prototypical TINRs including Bi_2Te_3 [40] and Bi_2Se_3 [41]. Note that a nanoribbon in this notation refers to a nanowire with a rectangular cross-section.

In the TINRs, the confinement of the surface states along the circumference will result in discretisation of modes around the circumference (we define this direction to be along the y axis as shown in Fig. 7.5a). Unlike conventional metallic hollow cylinders, the spin-helical nature of TSS in the TINRs ensures that the spin of carriers is always tangential to the surface and perpendicular to the momentum. This spin-momentum locking enforces a particle moving around the perimeter of the TINR to pick up an additional AB phase (Berry phase of π). In other words, we must use anti-periodic boundary conditions for TINRs when we consider the quantisation of the transversal modes. Therefore, the transversal modes in TINRs are described as follows [36,37]:

$$k_{y,n} = \frac{2\pi}{C}\left(n + \frac{1}{2}\right), \tag{7.2}$$

where $k_{y,n}$ is the transverse momentum along the circumference corresponding to n, C is the circumference of the TINR and n is an integer. For

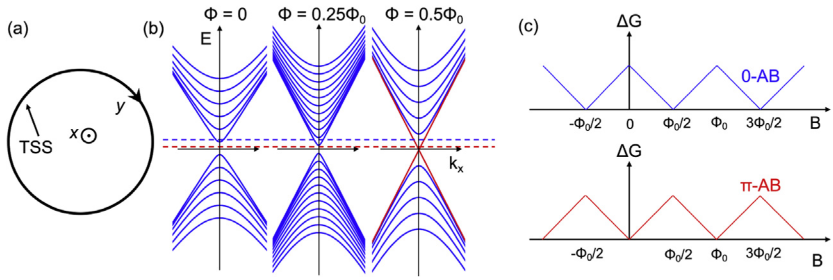

Figure 7.5 (a) Cross-section of a TI nanoribbon. We define y direction along the circumference and longitudinal *x* direction along the nanoribbon length. (b) Energy dispersion of the TI nanoribbon surface modes (E versus longitudinal momentum k_x) for three magnetic fluxes. (c) The predicted magnetoconductance ΔG versus B exhibiting Aharonov–Bohm (AB) oscillations with phase of 0 (blue [dark grey in print version] curve) and π (red [grey in print version] curve). 0-AB (π-AB) oscillations correspond to the Fermi energy E_F, as shown by the dashed blue (dark grey in print version) (red [grey in print version]) horizontal line in (B). *Credit: Reproduced from Ref. [42].*

any given k_y mode, the energy dispersion is also described using the linear Dirac dispersion as follows:

$$E_n(k_x) = \pm \hbar v_F \sqrt{k_x^2 + k_{y,n}^2}, \tag{7.3}$$

where k_x is the longitudinal momentum along the length of the TINR and v_F is the Fermi velocity of surface modes. When an axial magnetic field is applied, the electron wavefunction will pick up an additional AB phase of $2\pi\Phi/\Phi_0$ and quantised transverse modes will take the form of [36,37,42]

$$k_{y,n} = \frac{2\pi}{C}\left(n + \frac{1}{2} - \frac{\Phi}{\Phi_0}\right), \tag{7.4}$$

where $\Phi = B/S$ is the magnetic flux and S is the cross-sectional area of the TINR. Fig. 7.5b plots the energy dispersion of various k_y modes as a function of k_x for three different magnetic fluxes. Unique to the TINR, the energy dispersion is gapped at zero magnetic flux as well as at even multiples of $\Phi_0/2$. This is a result of the quantum confinement effect along the circumference. As the flux deviates from even multiples of $\Phi_0/2$, the energy gap decreases and closes at odd multiples of $\Phi_0/2$, restoring the linear Dirac dispersion. Therefore, an axial magnetic flux drives a periodic topological transition of the surface modes, from a system with all topologically trivial doubly degenerate transversal modes at even multiples of $\Phi_0/2$ to a system with a single nondegenerate mode for $k_y = 0$ and doubly degenerate modes for $k_y > 0$ at odd multiples of $\Phi_0/2$. The one-dimensional mode at $k_y = 0$ is spin helical with linear energy–momentum dispersion and is topologically protected against backscattering by nonmagnetic impurities. The energy gap between the two adjacent modes at $k_x = 0$ is also given by $\Delta E = \hbar v_F \Delta k_y$, where $\Delta k_y = k_{y,n+1} - k_{y,n} = 2\pi/C$ [42].

The unique magnetic flux dependence of the energy dispersion has an interesting consequence in the gate tunable magnetoconductance of the TINR. Let us take a look at the case where the chemical potential (controlled by the gate voltage) is tuned to the red (grey in print version) dashed line in Fig. 7.5b. At $T = 0$ K, the magnetoconductance of the TINR will be larger at $\Phi = (n + 1/2)\Phi_0$ compared to $\Phi = (2n)\Phi_0/2$, because at $\Phi = (n + 1/2)\Phi_0$, the topological mode at $k_y = 0$ will contribute to the conductance, whereas at $\Phi = (2n)\Phi_0/2$, the chemical potential is inside the gap and there is no mode to contribute to the conductance. Therefore, the magnetoconductance will have maxima at $(n + 1/2)\Phi_0$ and minima at $(n)\Phi_0$. A schematic representation of this type of AB oscillation (π-AB) is shown in Fig. 7.5c. Unlike the conventional AB effects, where magnetoconductance maxima are at zero and even multiples of $\Phi_0/2$ (Fig. 7.5c blue [grey in print version] curve), for the TINR at this specific gate voltage, the 1D topological mode gives rise to a π phase shift in the AB oscillations. This phenomenon is called the π-AB effect and is a result of the additional π phase shift introduced by the spin rotation of the 1D topological mode around the perimeter of the TINR. If we change the position of the chemical potential, for instance, to the dashed blue (dark grey in print version) line in Fig. 7.5b, at $\Phi = (2n)\Phi_0/2$, there are two modes contributing to the transport, whereas at $\Phi = (2n + 1)\Phi_0/2$, there is only one mode. We note here that all the modes in Fig. 7.5b are doubly degenerate except for the topological mode with the linear energy dispersion. Therefore, the magnetoconductance for this chemical potential will have maxima at even multiples of $\Phi_0/2$ and minima at odd multiples of $\Phi_0/2$. This type of magnetoconductance oscillations resembles the conventional AB effect (0-AB) without any phase shift, as shown with the blue (dark grey in print version) curve in Fig. 7.5c. Therefore, in the TINR, we can alternate the phase of the AB oscillations by changing the chemical potential of the TINRs. This 0 to π transition is periodic with respect to k_F with a period of $\Delta k_y = 2\pi/C$, which determines the energy separation (ΔE) of the modes at $k_x = 0$. We note that, experimentally, the temperature broadening and

Fermi energy fluctuations along the length of the nanoribbon should be smaller than the energy gap ΔE between the adjacent modes in Fig. 7.5b. The π-AB oscillations of the magnetoconductance were experimentally measured in Bi_2Se_3 nanoribbons in Ref. [43]. Jauregui et al. [42] reproduced the π-AB oscillations in Bi_2Te_3 nanoribbons and further demonstrated a clear periodic 0 to π alternation with respect to k_F, driven by the gate voltage. Fig. 7.6a and b summarises the experimental results corresponding to Ref. [42]. The gate-tunable AB oscillations are analysed by labelling each peak (dip) in the magnetoconductance at $\Phi = \Phi_0/2$ ($\Phi = 0$) with an integer (N). This procedure is done for back-gate voltages above V_0, where

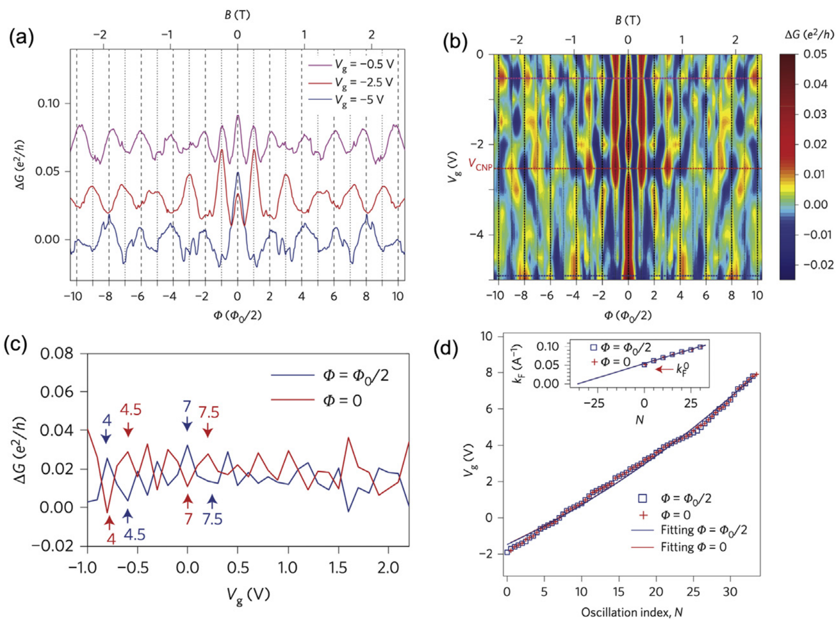

Figure 7.6 (a) Magnetoconductance (ΔG, with a smooth background subtracted) as a function of the magnetic flux (Φ) at three back-gate voltage V_g's for Bi_2Te_3 nanoribbons. The nanoribbon exhibits a 0-AB effect at $V_g = -5$ V and a π-AB effect for $V_g = -2.5$ V. (b) Colour plot of ΔG as functions of Φ and V_g, exhibiting 0 to π transition of the AB oscillations with V_g, which controls the chemical potential. The transition from 0 to π is periodic with respect to Δk. (c) ΔG versus V_g for $\Phi = \Phi_0/2$ and $\Phi = 0$. The corresponding N and $N + 1/2$ indexes are marked in the figure. (d) Each back-gate voltage corresponding to each N or $N + 1/2$ from (c) is plotted as a function of the N. Inset: k_F versus N exhibiting a linear behavior. This linear behaviour reveals that the oscillations (N) are periodic with respect to k_F with a periodicity given by Δk_y. *Credit: Ref. [42].*

V_0 is the smallest gate voltage where a transition from 0- to π-AB oscillations is observed. Similarly, each dip (peak) in the magnetoconductance at $\Phi = \Phi_0/2$ ($\Phi = 0$) is labelled with $N + 1/2$. Fig. 7.6c plots the back-gate voltage (V_g) as a function of the extracted oscillation index (N). For a back-gated TINR, the sheet carrier density n_s is given by

$$n_s = C_{ox}\left(V_g - V_{CNP}\right)/e, \tag{7.5}$$

where C_{ox} is the parallel plate capacitance of the oxide layer per unit area. Moreover, for a 2D band, the carrier density is also given by the following:

$$n_s = \left(k_F^2 - k_{F,0}^2\right)/4\pi, \tag{7.6}$$

where k_F is the Fermi wavevector of the surface modes and $k_{F,0}$ is the Fermi wavevector in the bulk valence band. We note that in our description, the TSS of the TINR is treated as a 2D plane with anti-periodic boundary conditions, and hence a 2D carrier density can properly describe the system. Assuming $k_F = k_{F,0} + N\Delta k_y$ with $\Delta k_y = 2\pi/C$, $k_{F,0}$ and C_{ox} can be extracted by fitting Eqs. (7.5) and (7.6) to V_g versus N data plotted in Fig. 7.6d. From this fit, $k_{F,0} \sim 0.05$ Å^{-1} and $C_{ox} \sim 100$ nF/cm^2 (for $SrTiO_3$ substrate) are obtained. To see the periodic nature of the oscillation index N with respect to k_F, the calculated $k_F = \sqrt{4\pi C_{ox}/e(V_g - V_0) + k_{F,0}^2}$ is plotted as a function of N in Fig. 7.6d. For $k_F < k_{F,0}$ ($V_g < V_0$), the magnetoconductance is dominated by the bulk valence band conduction, carriers are not localised to the TSS, and no AB oscillations are observed.

As we discussed earlier, at $T = 0$ K and for the dashed red (grey in print version) line in Fig. 7.5b, the conductance oscillations are due to the ballistic spin-helical TSS. Considering the ballistic nature of the $k_y = 0$ mode, one would expect the amplitude of the AB oscillations to be e^2/h, i.e., ideally the amplitude of ΔG in Fig. 7.6a should be quantised (e^2/h). However, all the experimentally measured AB oscillations in the TINRs [40–43] reported $\Delta G \sim 0.1e^2/h$, which is significantly smaller than the theoretically expected value. The exact mechanism giving rise to the reduction of the AB amplitude is not clear, even though disorder and temperature broadening as well as invasive contacts, whose reflection and transmission coefficients can influence the four-terminal magnetoconductance measurements, have been considered as the underlying reasons.

3.1 Ballistic transport from the temperature dependence of AB oscillations

The other interesting property of AB oscillations is their temperature dependence. The AB effect will have a different characteristic temperature dependence depending on whether transport is ballistic or diffusive [44]. Previous studies have shown that the amplitude of the AB oscillations in the diffusive regime exhibits a $T^{-1/2}$ dependence [40,41], whereas temperature dependence is exponential for ballistic nanoribbons [45]. In the TINRs, the amplitude of AB oscillations of the magnetoconductance is determined by the 1D topological mode with $k_y = 0$. Since this mode is topologically protected against backscattering, we expect to observe an exponential T-dependence of the AB amplitude. Fig. 7.7a depicts a colour

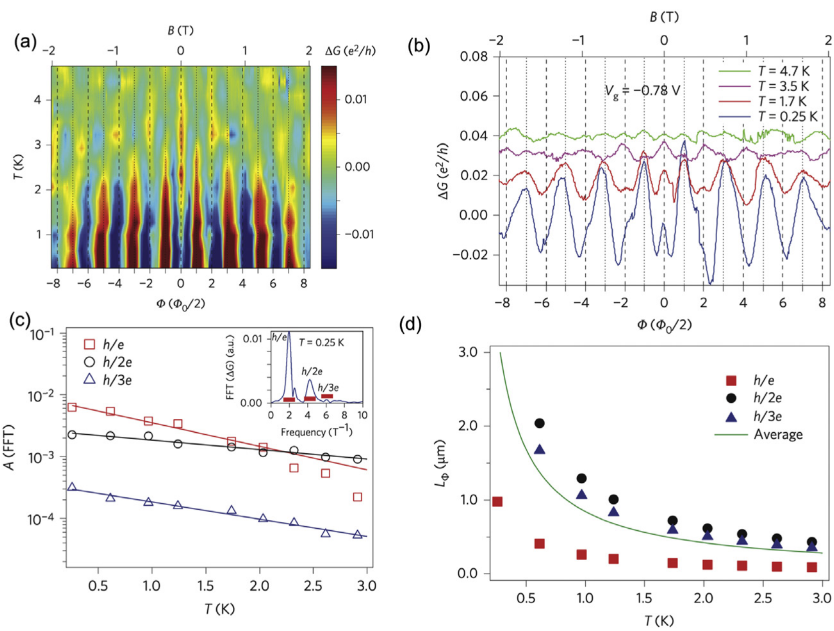

Figure 7.7 (a) Magnetoconductance (ΔG) versus temperature and magnetic flux in Bi_2Te_3 nanoribbons. (b) A few cuts of ΔG versus Φ of (a) for different temperatures. (c) temperature dependence of FFT amplitude A for the first (h/e), second ($h/2e$) and third ($h/3e$) harmonics. Inset is the FFT of the data of (b) at $T = 0.25$ K. The peak amplitude (A) is defined as the integrated area over the corresponding interval represented by the red (light grey in print version) horizontal line. (d) Temperature dependence of the phase coherence length (L_φ) obtained from $L_\varphi = jC/2Tb_j$, where j is the j^{th} harmonic in (c) and b_j is obtained from fitting A to e^{-b_jT}. l_φ exhibits T^{-1} dependence. An average between the three data sets is shown as a solid green (grey in print version) line. *Credit: Ref. [42].*

map plot of magnetoconductance in Bi_2Te_3 nanoribbon as functions of an axial magnetic field and temperature [42]. The amplitude of AB oscillations, corresponding to the first, second and third harmonics obtained from a fast Fourier transfer (FFT) of the data in (a), are also plotted in Fig. 7.7b. The amplitude of all three harmonics shows an exponential decay with the increasing temperature, revealing the ballistic nature of transport along the TINR length. Theoretically, the amplitude of FFT (A_j), where j is the j^{th} harmonic, is proportional to $e^{-b_j T}$, where the decay factor (b_j) is found to be $b_j = jC/(2Tl_\varphi)$ [45,46] and l_φ is the phase coherence length. Experimentally, it is found that b_j is a nonlinear function of j. Although the underlying origin of this deviation from a linear behaviour is not well established, similar deviations were attributed to thermal averaging. An extracted $l_\varphi = jC/(2Tb_j)$ displays a T^{-1} dependence [42]. This -1 exponent differs from 0.4 to 0.5 observed in Refs. [41,47–49] and, most likely, indicates weaker coupling of the TINRs to the environment [44].

4. Superconducting transport in TI nanoribbons

The TSSs are topologically nontrivial at zero magnetic field and, thus, TI/superconductor (TI/S) heterostructures are ideal to form a topological superconducting phase. Many theoretical works have studied the existence of Majorana modes in 3D TIs [16,38,39,50–55]. Additionally, TI/S interfaces, including S/TI/S Josephson junctions, have been experimentally demonstrated by many groups [56–64]. Superconducting transport in TIs is usually studied in a Josephson geometry, where two closely spaced superconductors are placed on top of a TI flake to form a Josephson junction. Fu and Kane [16] first pointed out that the induced superconductivity in the TSSs can give rise to zero-energy Majorana excitations. These excitations are named Majorana modes because their mathematical formulation is identical to Majorana fermions. The energy dispersion of the surface states in TIs is

$$E(k_F) = \pm \hbar v_F |k_F|. \tag{7.7}$$

This band structure is ideal to form a topological superconducting phase (which gives rise to the Majorana modes), because for any chemical potential inside the bulk gap, the spin-helical 'spinless' regime is automatically accessed, and the TI/S interface is topologically nontrivial at zero magnetic field [16,39]. In contrast, in semiconductor nanowires the spin-helical states emerge at large magnetic fields [65–70].

Fu and Kane [16] derived the following energy-phase relation for the Andreev bound states in a zero length Josephson junction (JJ):

$$E(\phi) = \pm \Delta_0 \cos\frac{\phi}{2}, \tag{7.8}$$

where Δ_0 is the superconducting gap at zero temperature, and ϕ is the phase difference across the JJ. Olund et al. [54] studied the effect of the channel length and of the out-of-gap states on the supercurrent; they derived

$$E(\phi) = \pm \Delta_0 \cos\left(\frac{E(\phi)L}{\hbar v_F} \pm \frac{\phi}{2}\right), \tag{7.9}$$

where L is the channel length, for a JJ with an arbitrary channel length. Expression (7.9) becomes (7.8) in a short-channel limit $L \to 0$. Ghaemi et al. [71] studied the effect of impurities; they found that the presence of impurities will act as an effective increase of the channel length, replacing L with L_{eff} in (7.9). Current phase relation (CPR) can be calculated by taking derivative of the energy with respect to the phase:

$$I\left(k_y, \phi\right) = -\frac{e}{h} \sum_{E_n \geq 0} \frac{\partial E_n}{\partial \phi} \tanh\frac{E_n}{2k_B T}. \tag{7.10}$$

Eq. (7.10) is derived assuming that the temporal changes of ϕ are slow. Hence, the Fermi distribution function (the tanh term) is included to account for this slow varying phase. Fig. 7.8a and b plot the energy spectrum of Andreev bound states and the corresponding CPR for topological and trivial junctions (transmission coefficient $D = 0.2$ is assumed for the trivial junction). Backscattering from nonmagnetic impurities is prohibited for TSS, which leads to the energy levels crossing at $\phi = \pi$, and, consequently, a 4π-periodic CPR [16]. In conventional JJs, the CPR is 2π-periodic [72]. The two energy branches have different fermion parity, and in order to measure 4π periodicity, the measurements have to be performed faster than the quasi-particle poisoning time [73]. In the presence of quasi-particle poisoning, the CPR of a topological JJ is expected to be skewed (due to the ballistic transport) but 2π periodic. In a short trivial junction, the energy-phase relation is given by [72]:

$$E(\phi) = \pm \Delta_0 \sqrt{1 - D \sin^2\frac{\phi}{2}}, \tag{7.11}$$

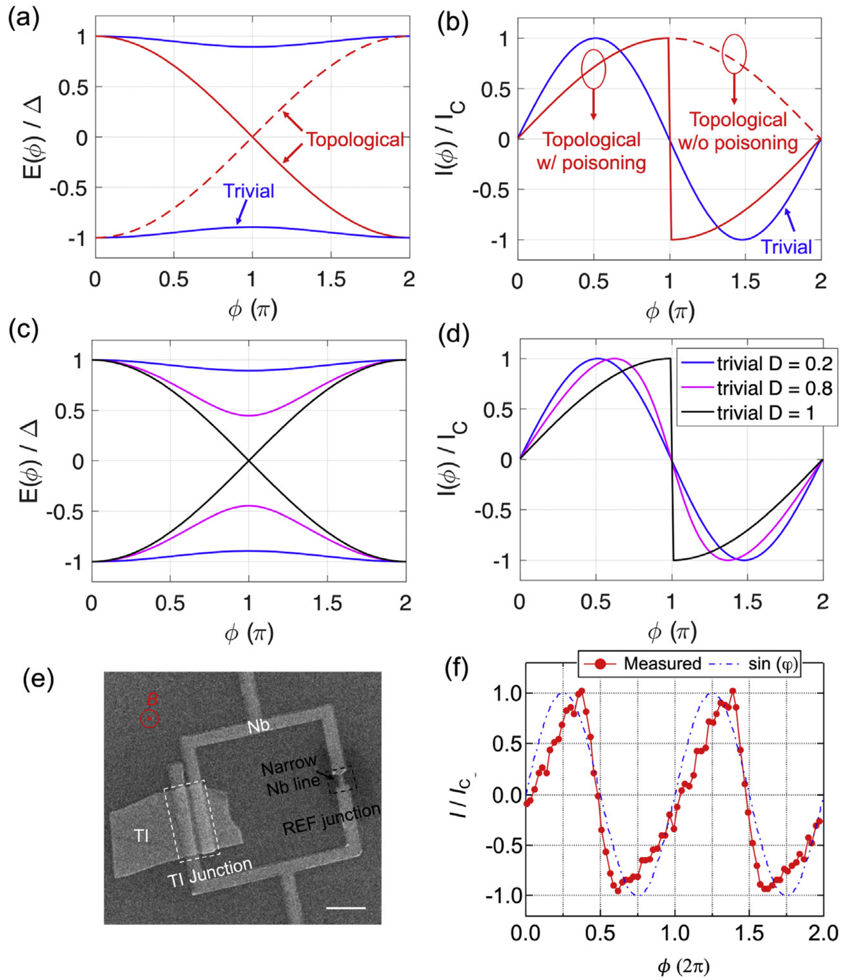

Figure 7.8 (a) Energy spectrum E of the Andreev bound states (ABS) versus the phase difference ϕ between the two superconductors in topological (red curve) and trivial (blue curve) Josephson junctions. (b) The current I, normalised by I_c (the critical current) versus ϕ for topological (red [grey in print version] solid and dashed curves) and trivial (blue [dark grey in print version] curve) junctions. Because of the quasi-particle poisoning, the topological junction may exhibit a highly skewed two π periodic $I - \phi$ [73]. (c,d) The energy spectrum E (c) and the normalised current I/I_c (d) in a trivial junction for various junction transparencies D. (e) A scanning electron microscope (SEM) image of an asymmetric superconducting quantum interference device (SQUID) used to measure the current phase relation (CPR). Scale bar is 1 μm. (f) The current phase relation (symbols): the normalised current (I/I_C) of the TI-based JJ versus the phase ϕ measured at temperature $T = 20$ mK. Dashed blue (grey in print version) curve is a reference sinusoidal function. *Credit: (e) and (f) are taken from Ref. [64].*

where D is the junction transparency. In Fig. 7.8c and d $E-\phi$ and $I-\phi$ are plotted for three trivial junctions with different transparencies D. For a perfectly ballistic junction, $E-\phi$ and $I-\phi$ curves resemble those of the topological junction with quasi-particle poisoning (slow varying phase). Therefore, observation of highly skewed CPR, even though a necessary step, is not sufficient evidence for the existence of topological superconductivity. In fact, to reveal the 4π-periodic nature of the CPR high frequency measurements, with frequencies above the quasi-particle poisoning rate, are required.

The CPR of the TI JJ can be measured in an asymmetric quantum interference device (SQUID), shown in Fig. 7.8e. The asymmetric SQUID consists of a reference (REF) junction with a known sinusoidal CPR in parallel with a TI-based junction. If the critical current of the REF junction is much larger than that of the TI junction, the magnetic flux modulation of the SQUID critical current will directly probe the CPR of the TI JJ. We have measured the CPR of $BiSbTeSe_2$ flakes using this technique; the results are plotted in Fig. 7.8f. We observe that the CPR is highly skewed, which is consistent with our understanding of ballistic TSS with a slow varying ϕ (controlled by the magnetic flux threading the SQUID) [64]. In contrast, in a TINR the $k_y=0$ 1D surface mode only appears at $\Phi=\left(n+\frac{1}{2}\right)\Phi_0$ and, hence, CPR in zero magnetic field is not expected to be 4π periodic.

4.1 Temperature dependence of the critical current in TI nanoribbons

Temperature dependence of the critical current I_c, which is the maximum value of $I(\phi)$ in Eq. (7.10) at any given temperature, is a versatile probe to study the induced superconductivity. $I_c(T)$ dependence has been investigated in S/TI/S JJs based on $BiSbTeSe_2$ nanoribbons with Nb as superconducting leads [61,63]. The $I_c(T)$ reveals an anomalous enhancement of the critical current at temperatures below $0.2T_c$, where T_c is the critical temperature of the JJ. We will refer to this transition temperature as T^*. Fig. 7.9a displays I_c versus T in a TINR at three different back-gate voltages. Starting from T_c, I_c increases smoothly with reducing temperature down to T^*, below which I_c exponentially increases as T approaches zero. In general, any model which considers two characteristic energy gaps in the system

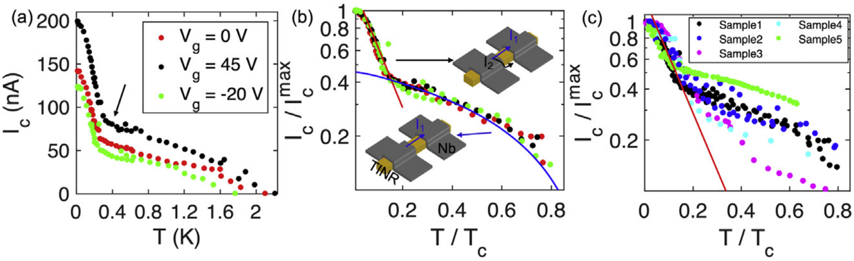

Figure 7.9 (a) Temperature dependence of I_c for different back-gate voltages (V_g's) in $BiSbTeSe_2$ nanoribbons. (b) Normalised I_c/I_c^{max} versus normalised T/T_c in a log-linear scale. The solid blue (dark grey in print version) curve is a fit to the short junction model and the solid red (grey in print version) curve is an exponential fit. Inset: cartoon of the TI nanoribbon junction depicting I_1 and I_2. (c) I_c/I_c^{max} versus T/T_c in a log-linear scale for five different $BiSbTeSe_2$ nanoribbons. Solid line is an exponential fit. *Credit: Ref. [63].*

can reproduce our observed temperature dependence. In the original paper [68], T^* was associated with superconductivity being induced into the bottom surface of the nanoribbon (the side which is not in contact with Nb), consistent with the observation that for $T < T^*$ Little–Park oscillations (discussed below) are observed [66]. The observed I_c versus T is radically different from that of the *short* JJs, where I_c saturates at low temperatures without exhibiting any exponential behaviour [72,74]. In contrast, for *long* JJs, I_c increases exponentially with decreasing temperature [72,75–78]. We note that short refers to a junction with $L \ll \xi$, where ξ is the superconducting phase coherence length, whilst $L \geq \xi$ is considered a long junction. The model assumes that the increase in I_c versus decreasing T for $T^* < T \leq T_c$ followed by an exponential enhancement of I_c for $T < T^*$ as observed in Fig. 7.9 accounts for a transition from a short to long junction limit at T^*, where superconductivity extends to the bottom TSS. The total current $I = I_1 + I_2$ is carried by the top TSS (I_1 in the inset of Fig. 7.9b) and by the bottom TSS (I_2). The supercurrent corresponding to I_2 involves modes with large k_y that extend around the circumference and go from the top left superconductor to the top right one. The circumference of the nanoribbon $C \geq \xi$ and these modes are in the long junction regime. I_1 is governed by modes with small k_y, which are in a ballistic regime, and is well described by Eq. (7.10). I_2 has an exponential T-dependence [72,78]:

$$I_2 \propto \exp\left(-\frac{k_B T}{\delta}\right), \tag{7.12}$$

where δ is the characteristic energy gap of the modes in the long junction and is given by

$$\delta = \frac{\hbar v_F}{2\pi d}, \tag{7.13}$$

where d is the effective length. I_2 becomes appreciable for small $T < \delta / k_B$. From the fit to experimental data, we extract $\delta \sim 0.08\Delta_0$, corresponding to the effective length of $d = 1.2$ μm, twice larger than $C \sim 0.7$ μm. This anomalous temperature enhancement has been observed in multiple $BiSbTeSe_2$ nanoribbon JJs (see Fig. 7.9c). Yet another theoretical explanation to the observed temperature dependence was put forward by Talantsev [79], who argues that the sharp transition in $I_c - T$ curves might be related to the linear Dirac energy dispersion of the TINR rather than the winding of the TSS. Future theoretical and experimental investigations might be needed to clarify the origin of anomalous critical current enhancement at low temperatures.

4.2 Aharonov–Bohm effect in TI nanoribbon Josephson junctions

In the presence of an axial magnetic field, the critical current in the junction is expected to exhibit AB oscillations, similar to the conductance oscillations in the normal state discussed earlier. Because of the unique quantisation of the transverse momentum k_y (Eq. 7.4) and the band dispersion in the TINR, a transition between 0- and π-AB effect is also predicted to occur in the superconducting state [38,39,51,80,81]. In the superconducting state, oscillations are due to the interference of Cooper pairs with charge $2e$ and flux is quantised in units of $\Phi_{s0} = h/2e$, half the flux in the normal state (this phenomenon is also known as the Little–Park effect). In the presence of ballistic Andreev bound states, including Majorana bound states, oscillations with h/e period are predicted [51,82].

Fig. 7.10 shows a nanoribbon device with four normal (N, Ti/Au) and four superconducting (S, Nb) contacts [83]. For N contacts, the AB oscillations with a period $\Delta B_n = 0.48$ T are observed. The phase of the AB oscillations changes from π for $V_g = 14.5$ V to 0 for $V_g = 16$ V and back to π for $V_g = 17.5$ V, similar to the AB oscillations discussed earlier (Fig. 7.7). This gate-induced periodic $\pi - 0 - \pi$ transition unambiguously confirms TSS transport in this TI nanoribbon. Now we compare AB oscillations in the normal regime with oscillations of the critical current in a JJ formed between two S contacts in the same nanoribbon. In Fig. 7.10c, differential

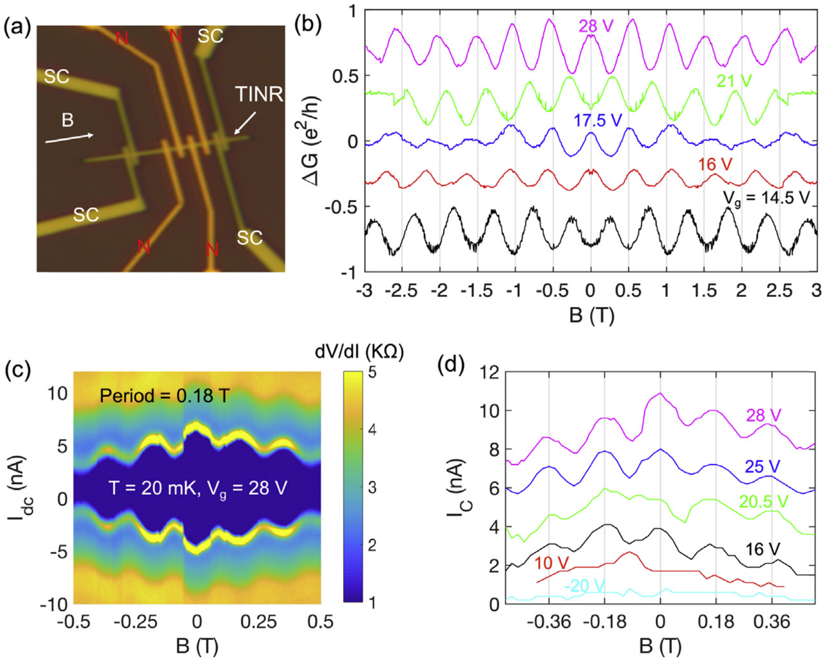

Figure 7.10 (a) An optical microscope image of the TI nanoribbon with Ti/Au normal (N) contacts and Nb superconducting (SC) contacts. (b) Magnetoconductance ΔG versus the axial magnetic field measured using the normal contacts for various back-gate voltages (V_g's) at $T = 20$ mK. Curves are shifted vertically for clarity. (c) Colour map of the two-terminal differential resistance dV/dI as functions of I_{dc} and B measured at $V_g = 28$ V and $T = 20$ mK. (d) The critical current I_c versus B measured for different V_g's at $T = 20$ mK. Quantum interference patterns in I_c with period of $\Delta B_s \sim 0.18$ T are observed. *Credit: Ref [83].*

resistance is plotted as a function of dc current I_{dc} and the magnetic field B at $T = 20$ mK and $V_g = 28$ V for a JJ. The blue (light grey in print version) region corresponds to the $R = 0$ state, and its boundary (I_c) oscillates with magnetic field. In Fig. 7.10d, oscillations of I_c versus the axial magnetic field are plotted for several gate voltages. Three features stand out in the superconducting transport: first, the interference patterns are AB-like (or SQUID-like) and, hence, are different from the Fraunhofer patterns measured in the perpendicular magnetic fields. Second, the period of the oscillations is $\Delta B_s \sim 0.18$ T, which is > 2 times smaller than the period of 0.48 T in the normal state. The fact that $\Delta B_s \lesssim \Delta B_n/2$ may suggest that oscillations are due to Cooper pair interference. There are however several other possible factors that can contribute to the period reduction in the S state, including magnetic flux focusing and supercurrent extending to the outer surface of Nb contacts, thus effectively increasing the enclosed area. Third, the phase of the supercurrent oscillations remains zero regardless of the applied gate voltage. It is not clear why the π-AB oscillations do not show up in the superconducting state. However, we speculate that superconducting condensate is very effective in screening the gate field and, thus, the gate is not as efficient in tuning the Fermi level in superconducting state. Overall, the AB-like quantum interference patterns observed in the TINR provide yet another signature of the surface superconductivity. We note here that further experimental investigation, e.g., direct measurement of the 4π-periodic CPR, is necessary to conclude whether topological superconductivity and Majorana modes can indeed exist in the TINR-based Josephson junctions.

5. Summary and outlook

In this chapter we summarised recent progress in electrical and superconducting transport of TINRs. In particular, we analysed signatures of topological transport in temperature and magnetic field dependence of the electrical conductivity and the supercurrent. Furthermore, AB interferences of TSSs were discussed in both normal and superconducting states. These signatures provide strong evidence for the existence of TSS and importance of TSS transport in TINRs. The TSSs have already found applications in spintronics, and TI/S hybrid structures are one of the prime candidates for the observation of the Majorana modes, which are predicted to exhibit non-Abelian statistics. Despite significant efforts over the past decade, Majorana modes have not been conclusively observed. Further progress may require higher quality TIs (fewer bulk states, lower disorder and reduced amount of impurities) and cleaner, more transparent TI/S interfaces. YPC and LPR acknowledge partial support by Quantum Science Center (QSC), a US Department of Energy (DOE) National Quantum Information Science Research Center, during the writing of this chapter.

References

[1] Hasan MZ, Kane CL. *Colloquium*: topological insulators. Rev Mod Phys 2010;82: 3045–67.
[2] Qi X-L, Zhang S-C. Topological insulators and superconductors. Rev Mod Phys 2011;83:1057–110.
[3] Maciejko J, Hughes TL, Zhang S-C. The quantum spin Hall effect. Annu Rev Condens Matter Phys 2011;2:31–53.

[4] Ando Y, Fu L. Topological crystalline insulators and topological superconductors: from concepts to materials. Annu Rev Condens Matter Phys 2015;6:361–81.
[5] Yan B, Felser C. Topological materials: Weyl semimetals. Annu Rev Condens Matter Phys 2017;8:337–54.
[6] Armitage NP, Mele EJ, Vishwanath A. Weyl and Dirac semimetals in three-dimensional solids. Rev Mod Phys 2018;90:015001.
[7] Moore JE. The birth of topological insulators. Nature 2010;464:194–8.
[8] Goldsmid HJ. Introduction to thermoelectricity. 2nd ed. Springer; 2010.
[9] König M, Molenkamp LW, Qi X, Zhang S. Quantum spin Hall insulator state in HgTe quantum wells. Science 2007;318:766–71.
[10] Wolgast S, Kurdak Ç, Sun K, Allen JW, Kim DJ, Fisk Z. Low-temperature surface conduction in the Kondo insulator SmB_6. Phys Rev B 2013;88:180405.
[11] Fan Y, Wang KL. Spintronics based on topological insulators. Spin 2016;6:1640001.
[12] Tian J, Hong S, Miotkowski I, Datta S, Chen YP. Observation of current-induced, long-lived persistent spin polarization in a topological insulator: a rechargeable spin battery. Sci Adv 2017;3:e1602531.
[13] Yu R, Zhang W, Zhang H-J, Zhang S-C, Dai X, Fang Z. Quantized anomalous Hall effect in magnetic topological insulators. Science 2010;329:61–4.
[14] Chang C-Z, Zhang J, Feng X, Shen J, Zhang Z, Guo M, Li K, Ou Y, Wei P, Wang L-L, Ji Z-Q, Feng Y, Ji S, Chen X, Jia J, Dai X, Fang Z, Zhang S-C, He K, Wang Y, Lu L, Ma X-C, Xue Q-K. Experimental observation of the quantum anomalous Hall effect in a magnetic topological insulator. Science 2013;340:167–70.
[15] Qi X-L, Hughes TL, Zhang S-C. Topological field theory of time-reversal invariant insulators. Phys Rev B 2008;78:195424.
[16] Fu L, Kane CL. Superconducting proximity effect and Majorana fermions at the surface of a topological insulator. Phys Rev Lett 2008;100:096407.
[17] Xia Y, Qian D, Hsieh D, Wray L, Pal A, Lin H, Bansil A, Grauer D, Hor YS, Cava RJ, Hasan MZ. Observation of a large-gap topological-insulator class with a single Dirac cone on the surface. Nat Phys 2009;5:398–402.
[18] Ren Z, Taskin AA, Sasaki S, Segawa K, Ando Y. Large bulk resistivity and surface quantum oscillations in the topological insulator Bi2 Te2 Se. Phys Rev B 2010;82: 241306.
[19] Taskin AA, Ren Z, Sasaki S, Segawa K, Ando Y. Observation of Dirac holes and electrons in a topological insulator. Phys Rev Lett 2011;107:016801.
[20] Xiong J, Luo Y, Khoo Y, Jia S, Cava RJ, Ong NP. High-field Shubnikov-de Haas oscillations in the topological insulator Bi_2 Te_2 Se. Phys Rev B 2012;86:045314.
[21] Arakane T, Sato T, Souma S, Kosaka K, Nakayama K, Komatsu M, Takahashi T, Ren Z, Segawa K, Ando Y. Tunable Dirac cone in the topological insulator Bi_2-xSb xTe_3-ySey. Nat Commun 2012;3:636.
[22] Xu Y, Miotkowski I, Liu C, Tian J, Nam H, Alidoust N, Hu J, Shih C-K, Hasan MZ, Chen YP. Observation of topological surface state quantum Hall effect in an intrinsic three-dimensional topological insulator. Nat Phys 2014;10:956–63.
[23] Gao BF, Gehring P, Burghard M, Kern K. Gate-controlled linear magnetoresistance in thin Bi_2Se_3 sheets. Appl Phys Lett 2012;100:212402.
[24] Hikami S, Larkin AI, Nagaoka Y. Spin-orbit interaction and magnetoresistance in the two dimensional random system. Prog Theor Phys 1980;63:707–10.
[25] Xu Y. Quantum transport in three-dimensional topological insulators. Purdue University; 2019.
[26] Klitzing KV, Dorda G, Pepper M. New method for high-accuracy determination of the fine-structure constant based on quantized Hall resistaqnce. Phys Rev Lett 1980; 45:494–7.
[27] Girivin SM. Topological aspects of low dimensional systems. Springer; 2000.
[28] Prange RE, Girvin SM, Klitzing KV, editors. The quantum Hall effect. 2nd ed. Springer; 1989.

[29] den Nijs M. Quantized Hall conductance in a two dimensional periodic potential. Phys A Stat Mech Appl 1984;124:199–210.

[30] Laughlin RB. Quantized Hall conductivity in two dimensions. Phys Rev B 1981;23: 5632–3.

[31] Fu L, Kane CL. Topological insulators with inversion symmetry. Phys Rev B 2007;76: 045302.

[32] Yoshimi R, Tsukazaki A, Kozuka Y, Falson J, Takahashi KS, Checkelsky JG, Nagaosa N, Kawasaki M, Tokura Y. Quantum Hall effect on top and bottom surface states of topological insulator $(Bi_{1}1\text{-x}\ Sbx)_2\ Te_3$ films. Nat Commun 2015;6:6627.

[33] Zou W, Wang W, Kou X, Lang M, Fan Y, Choi ES, Fedorov AV, Wang K, He L, Xu Y, Wang KL. Observation of Quantum Hall effect in an ultra-thin $(Bi_{0.53}Sb_{0.47})_2Te_3$ film. Appl Phys Lett 2017;110:212401.

[34] Xu Y, Miotkowski I, Chen YP. Quantum transport of two-species Dirac fermions in dual-gated three-dimensional topological insulators. Nat Commun 2016;7:11434.

[35] Aronov AG, Sharvin YV. Magnetic flux effects in disordered conductors. Rev Mod Phys 1987;59:755–79.

[36] Zhang Y, Vishwanath A. Anomalous Aharonov-Bohm conductance oscillations from topological insulator surface states. Phys Rev Lett 2010;105:206601.

[37] Bardarson JH, Brouwer PW, Moore JE. Aharonov-Bohm oscillations in disordered topological insulator nanowires. Phys Rev Lett 2010;105:156803.

[38] Cook A, Franz M. Majorana fermions in a topological-insulator nanowire proximity-coupled to an s-wave superconductor. Phys Rev B 2011;84:201105.

[39] Cook AM, Vazifeh MM, Franz M. Stability of Majorana fermions in proximity-coupled topological insulator nanowires. Phys Rev B 2012;86:155431.

[40] Xiu F, He L, Wang Y, Cheng L, Te Chang L, Lang M, Huang G, Kou X, Zhou Y, Jiang X, Chen Z, Zou J, Shailos A, Wang KL. Manipulating surface states in topological insulator nanoribbons. Nat Nanotechnol 2011;6:216–21.

[41] Peng H, Lai K, Kong D, Meister S, Chen Y, Qi XL, Zhang SC, Shen ZX, Cui Y. Aharonov-Bohm interference in topological insulator nanoribbons. Nat Mater 2010; 9:225–9.

[42] Jauregui LA, Pettes MT, Rokhinson LP, Shi L, Chen YP. Magnetic field-induced helical mode and topological transitions in a topological insulator nanoribbon. Nat Nanotechnol 2016;11:345–51.

[43] Cho S, Dellabetta B, Zhong R, Schneeloch J, Liu T, Gu G, Gilbert MJ, Mason N. Aharonov–Bohm oscillations in a quasi-ballistic three-dimensional topological insulator nanowire. Nat Commun 2015;6:7634.

[44] Hansen AE, Kristensen A, Pedersen S, Sørensen CB, Lindelof PE. Mesoscopic decoherence in Aharonov-Bohm rings. Phys Rev B 2001;64:045327.

[45] Dufouleur J, Veyrat L, Teichgräber A, Neuhaus S, Nowka C, Hampel S, Cayssol J, Schumann J, Eichler B, Schmidt OG, Büchner B, Giraud R. Quasiballistic transport of Dirac fermions in a Bi_2Se_3 nanowire. Phys Rev Lett 2013;110:186806.

[46] Dragoman M, Konstantinidis G, Tsagaraki K, Kostopoulos T, Dragoman D, Neculoiu D. Graphene-like metal-on-silicon field-effect transistor. Nanotechnology 2012;23:305201.

[47] Ning W, Du H, Kong F, Yang J, Han Y, Tian M, Zhang Y. One-dimensional weak antilocalization in single-crystal $Bi_2\ Te_3$ nanowires. Sci Rep 2013;3:1564.

[48] Matsuo S, Koyama T, Shimamura K, Arakawa T, Nishihara Y, Chiba D, Kobayashi K, Ono T, Chang CZ, He K, Ma XC, Xue QK. Weak antilocalization and conductance fluctuation in a submicrometer-sized wire of epitaxial Bi_2Se_3. Phys Rev B Condens Matter 2012;85:075440.

[49] Hamdou B, Gooth J, Dorn A, Pippel E, Nielsch K. Aharonov-Bohm oscillations and weak antilocalization in topological insulator Sb_2Te_3 nanowires. Appl Phys Lett 2013; 102:223110.

[50] Ioselevich PA, Feigel'Man MV. Anomalous Josephson current via Majorana bound states in topological insulators. Phys Rev Lett 2011;106:077003.

[51] Ilan R, Bardarson JH, Sim HS, Moore JE. Detecting perfect transmission in Josephson junctions on the surface of three dimensional topological insulators. New J Phys 2014; 16:053007.

[52] Potter AC, Fu L. Anomalous supercurrent from Majorana states in topological insulator Josephson junctions. Phys Rev B 2013;88:121109.

[53] Tkachov G, Hankiewicz EM. Spin-helical transport in normal and superconducting topological insulators. Phys Status Solidi B 2013;250:215–32.

[54] Olund CT, Zhao E. Current-phase relation for Josephson effect through helical metal. Phys Rev B 2012;86:214515.

[55] Tkachov G. Magnetoelectric Andreev effect due to proximity-induced nonunitary triplet superconductivity in helical metals. Phys Rev Lett 2017;118:016802.

[56] Lee JH, Lee G-H, Park J, Lee J, Nam S-G, Shin Y-S, Kim JS, Lee H-J. Local and nonlocal Fraunhofer-like pattern from an edge-stepped topological surface Josephson current distribution. Nano Lett 2014;14:5029–34.

[57] Wiedenmann J, Bocquillon E, Deacon RS, Hartinger S, Herrmann O, Klapwijk TM, Maier L, Ames C, Brüne C, Gould C, Oiwa A, Ishibashi K, Tarucha S, Buhmann H, Molenkamp LW. 4π-periodic Josephson supercurrent in HgTe-based topological Josephson junctions. Nat Commun 2015;7:10303.

[58] Kurter C, Finck ADK, Hor YS, Van Harlingen DJ. Evidence for an anomalous current-phase relation in topological insulator Josephson junctions. Nat Commun 2015;6:7130.

[59] Xu J-P, Wang M-X, Liu ZL, Ge J-F, Yang X, Liu C, Xu ZA, Guan D, Gao CL, Qian D, Liu Y, Wang Q-H, Zhang F-C, Xue Q-K, Jia J-F. Experimental detection of a Majorana mode in the core of a magnetic vortex inside a topological insulator-superconductor $Bi_2Te_3/NbSe_2$ heterostructure. Phys Rev Lett 2015;114:017001.

[60] Sun H-H, Zhang K-W, Hu L-H, Li C, Wang G-Y, Ma H-Y, Xu Z-A, Gao C-L, Guan D-D, Li Y-Y, Liu C, Qian D, Zhou Y, Fu L, Li S-C, Zhang F-C, Jia J-F. Majorana zero mode detected with spin selective Andreev reflection in the vortex of a topological superconductor. Phys Rev Lett 2016;116:257003.

[61] Jauregui LALA, Kayyalha M, Kazakov A, Miotkowski I, Rokhinson LPLP, Chen YPYP. Gate-tunable supercurrent and multiple Andreev reflections in a superconductor-topological insulator nanoribbon-superconductor hybrid device. Appl Phys Lett 2018;112:093105.

[62] Ghatak S, Breunig O, Yang F, Wang Z, Taskin AA, Ando Y. Anomalous fraunhofer patterns in gated Josephson junctions based on the bulk-insulating topological insulator $BiSbTeSe_2$. Nano Lett 2018;18:5124–31.

[63] Kayyalha M, Kargarian M, Kazakov A, Miotkowski I, Galitski VM, Yakovenko VM, Rokhinson LP, Chen YP. Anomalous low-temperature enhancement of supercurrent in topological-insulator nanoribbon Josephson junctions: evidence for low-energy Andreev bound states. Phys Rev Lett 2019;122:047003.

[64] Kayyalha M, Kazakov A, Miotkowski I, Khlebnikov S, Rokhinson LP, Chen YP. Highly skewed current-phase relation in superconductor-topological insulator-superconductor Josephson junctions. Npj Quantum Mater 2020;5:7.

[65] Lutchyn RM, Sau JD, Das Sarma S. Majorana fermions and a topological phase transition in semiconductor-superconductor heterostructures. Phys Rev Lett 2010;105: 077001.

[66] Oreg Y, Refael G, von Oppen F. Helical liquids and Majorana bound states in quantum wires. Phys Rev Lett 2010;105:177002.
[67] Mourik V, Zuo K, Frolov SM, Plissard SR, Bakkers EPAM, Kouwenhoven LP. Signatures of Majorana fermions in hybrid superconductor-semiconductor nanowire devices. Science 2012;336:1003–7.
[68] Das A, Ronen Y, Most Y, Oreg Y, Heiblum M, Shtrikman H. Zero-bias peaks and splitting in an Al–InAs nanowire topological superconductor as a signature of Majorana fermions. Nat Phys 2012;8:887.
[69] Albrecht SM, Higginbotham AP, Madsen M, Kuemmeth F, Jespersen TS, Nygård J, Krogstrup P, Marcus CM. Exponential protection of zero modes in Majorana islands. Nature 2016;531:206–9.
[70] Zhang H, Liu C-X, Gazibegovic S, Xu D, Logan JA, Wang G, Van Loo N, Bommer JDS, De Moor MWA, Car D, Op Het Veld RLM, Van Veldhoven J, Koelling S, Verheijen MA, Pendharkar M, Pennachio DJ, Shojaei B, Lee JS, Palmstrøm CJ, Bakkers EPAM, Das Sarma S, Kouwenhoven LP. Quantized Majorana conductance. Nature 2018;556:74–9.
[71] Ghaemi P, Nair VP. Effect of impurities on the Josephson current through helical metals: exploiting a neutrino paradigm. Phys Rev Lett 2016;116:037001.
[72] Golubov AA, Kupriyanov MY, Il'ichev E. The current-phase relation in Josephson junctions. Rev Mod Phys 2004;76:411–69.
[73] Peng Y, Pientka F, Berg E, Oreg Y, von Oppen F. Signatures of topological Josephson junctions. Phys Rev B 2016;94:085409.
[74] Likharev KK. Superconducting weak links. Rev Mod Phys 1979;51:101–59.
[75] Dubos P, Courtois H, Pannetier B, Wilhelm FK, Zaikin AD, Schon G. Josephson critical current in a long mesoscopic S-N-S junction. Phys Rev B 2001;63:064502.
[76] Angers L, Chiodi F, Montambaux G, Ferrier M, Guéron S, Bouchiat H, Cuevas JC. Proximity dc squids in the long-junction limit. Phys Rev B 2008;77:165408.
[77] Ting Ke C, V Borzenets I, Draelos AW, Amet F, Bomze Y, Jones G, Craciun M, Russo S, Yamamoto M, Tarucha S, Finkelstein G. Critical current scaling in long diffusive graphene-based Josephson junctions. Nano Lett 2016;16:4788–91.
[78] V Borzenets I, Amet F, Ke CT, Draelos AW, Wei MT, Seredinski A, Watanabe K, Taniguchi T, Bomze Y, Yamamoto M, Tarucha S, Finkelstein G. Ballistic graphene Josephson junctions from the short to the long junction regimes. Phys Rev Lett 2016;117:237002.
[79] Talantsev. Classifying induced superconductivity in atomically thin Dirac-cone materials. Condens Matter 2019;4:83.
[80] de Juan F, Bardarson JH, Ilan R. Conditions for fully gapped topological superconductivity in topological insulator nanowires. SciPost Phys 2019;6:060.
[81] Bercioux D, Cayssol J, Vergniory MG, Calvo MR. Topological matter: lectures from the topological matter school 2017. Springer; 2018.
[82] Fornieri A, Amado M, Carillo F, Dolcini F, Biasiol G, Sorba L, Pellegrini V, Giazotto F. A ballistic quantum ring Josephson interferometer. Nanotechnology 2013;24:245201.
[83] Kayyalha M. Electrical, thermoelectric, and phase coherence transport in two-dimensional materials. PhD Dissertation. Purdue University; 2018.